Check for updates

ADVANCED MATERIALS
www.advmat.de

Convergence of Machine Vision and Melt Electrowriting

Pawel Mieszczanek, Thomas M. Robinson, Paul D. Dalton, and Dietmar W. Hutmacher**

Melt electrowriting (MEW) is a high-resolution additive manufacturing technology that balances multiple parametric variables to arrive at a stable fabrication process. The better understanding of this balance is underscored here using high-resolution camera vision of jet stability profiles in different electrical fields. Complementing this visual information are fiber-diameter measurements obtained at precise points, allowing the correlation to electrified jet properties. Two process signatures—the jet angle and for the first time, the Taylor cone area—are monitored and analyzed with a machine vision system, while SEM imaging for diameter measurement correlates real-time information. This information, in turn, allows the detection and correction of fiber pulsing for accurate jet placement on the collector, and the in-process assessment of the fiber diameter. Improved process control is used to successfully fabricate collapsible MEW tubes; structures that require exceptional accuracy and printing stability. Using a precise winding angle of 60° and 300 layers, the resulting 12 mm-thick tubular structures have elastic snap-through instabilities associated with mechanical metamaterials. This study provides a detailed analysis of the fiber pulsing occurrence in MEW and highlights the importance of real-time monitoring of the Taylor cone volume to better understand, control, and predict printing instabilities.

1. Introduction

Melt electrowriting (MEW) is an additive manufacturing (AM) technology that accurately direct-writes small diameter fibers onto a collector. What distinguishes MEW from the other melt extrusion-based AM technologies is the electrohydrodynamically-stabilized molten jet that achieves microscale resolutions of the fiber, from 0.8 to 50 microns.[1] Since an electric field between the nozzle and collector prevents Raleigh–Plateau instabilities at low flow rates during direct-writing,[2] a standard-sized nozzle can be used. With a nozzle deliberately raised above the collector, MEW has an ideal visual access point for in-processing monitoring during printing when compared to other AM technologies (**Figure 1**A,B; Videos S1–S4, Supporting Information). Especially for bespoke products, a 3D printing technology would ultimately require morphometric visual imaging to validate manufacture.[3]

Inspired by advancements from prototyping to manufacturing of metal-based AM, we recognize that a key factor for the effective transition within this technology was the implementation of machine vision (MV)—an in-process monitoring and analysis method that provides real-time data of the process.[4–7] For metal-based AM, this allowed to significantly improve the quality and reproducibility of the fabricated objects and parts[5,8,9] and therefore progress through technology readiness levels (TRLs). Therefore, the integration of MV into MEW should enable the technique to achieve a level of process control that is a condition sine qua non for delivering reproducible results and ultimately industrial applications (Figure S1, Supporting Information).

2. Results and Discussion

Previous visual analysis of the MEW jet flight path has provided the fundamental understanding of the printing process through experiments focusing on parameters and their effect on outcomes such as jet angle and printed fiber diameter.[10] From this, it was determined that applied pressure, high voltage (HV), and collector speed predominantly influence the fiber diameter[11] and process stability.[12] However, MEW is an inherently multiparametric[10] and also a user-dependant process. To produce a spectrum of well-defined fiber diameters across a large number of print layers, multiple parameters may require adjusting during printing.[13,14]

When the parameters are not in balance, a phenomenon called "fiber pulsing" results. This is a continuous oscillation of the jet volume that, in turn, affects fiber diameter and placement. Figure 1D,E and Video S2, Supporting Information are

P. Mieszczanek, T. M. Robinson, Prof. D. W. Hutmacher
Institute of Health and Biomedical Innovation
Queensland University of Technology
60 Musk Avenue, Kelvin Grove 4059, Australia
E-mail: dietmar.hutmacher@qut.edu.au
T. M. Robinson, Prof. P. D. Dalton
Department of Functional Materials in Medicine and Dentistry
and Bavarian Polymer Institute
Julius-Maximilians University of Würzburg
Pleicherwall 2, 97070 Würzburg, Germany
E-mail: paul.dalton@fmz.uni-wuerzburg.de
Prof. P. D. Dalton
Phil and Penny Knight Campus for Accelerating Scientific Impact
University of Oregon
1505 Franklin Boulevard, Eugene, OR 97403-6231, USA
E-mail: pdalton@uoregon.edu
The ORCID identification number(s) for the author(s) of this article can be found under https://doi.org/10.1002/adma.202100519.

© 2021 The Authors. Advanced Materials published by Wiley-VCH GmbH. This is an open access article under the terms of the Creative Commons Attribution-NonCommercial License, which permits use, distribution and reproduction in any medium, provided the original work is properly cited and is not used for commercial purposes.

DOI: 10.1002/adma.202100519

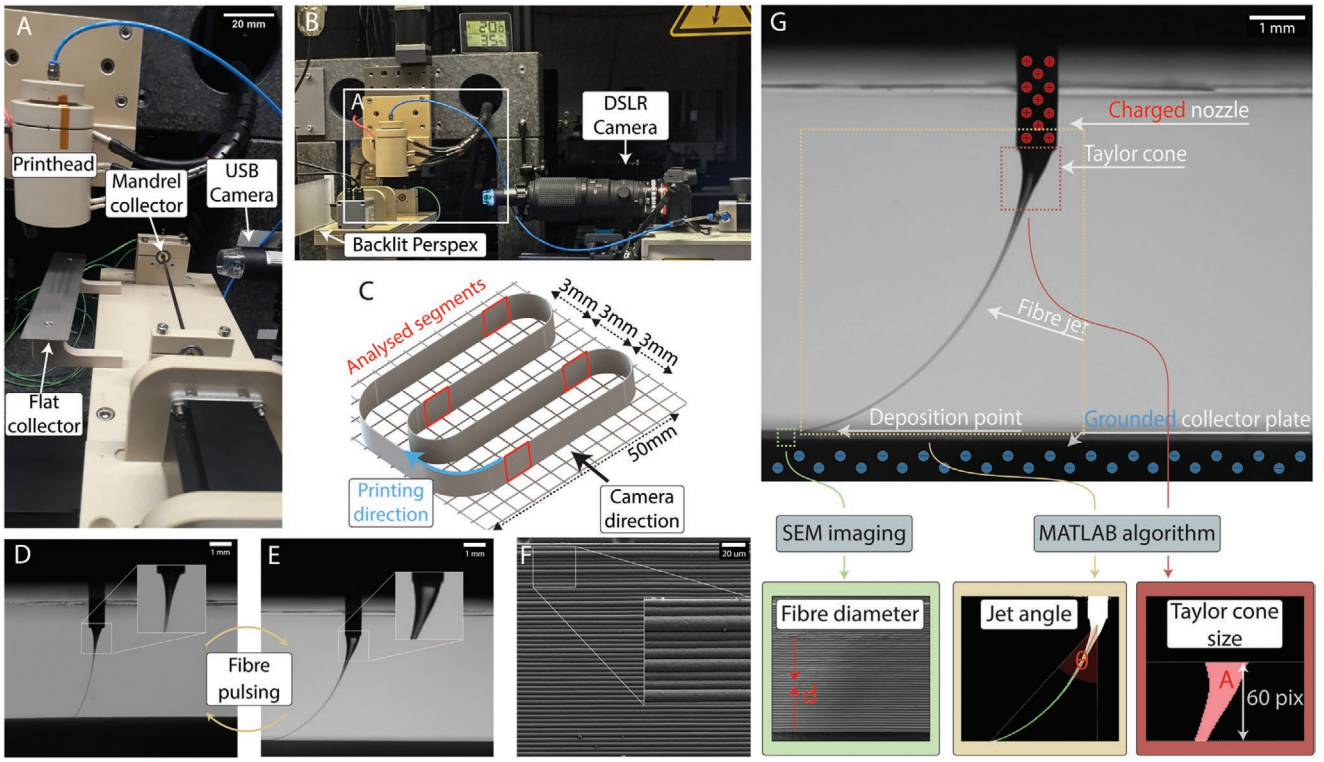

Figure 1. A) MEW printer consisting of both a flat and mandrel collector. B) The high-resolution camera is positioned out of field and behind the USB camera that is used for approximate positioning. C) Schematic of the experimental design, so that the exact timing of the MV can be correlated with fiber diameter measurements. D,E) Photographs of the MEW jet during fiber pulsing phenomenon with: D) a small Taylor cone volume associated with a smaller fiber diameter, that oscillates to E) a large Taylor cone volume, which results in larger fiber diameters and greater fiber jet lag. F) SEM imaging of the fiber wall showing the result of uncontrolled oscillating from (D) to (E) where different fiber diameters result. G) A single frame is captured from the video recording of the process, to analyze the process signatures of MEW. The fiber diameter is measured using SEM, while the jet angle and Taylor cone area are computed by analyzing specific regions using MATLAB.

examples where fiber pulsing leads to an inconsistent fiber diameter (Figure 1F). This study demonstrates that MV allows the capture and analysis of important, subtle, visual information to improve and expand on the precision capabilities of MEW.

The MEW jet stability was analyzed using four different electric field environments, with two air pressure levels of 0.4 and 0.7 bar for each group. As a control group, the HV and collector distance are not changed, which is traditionally used within most previous studies.[1,15–17] For thicker constructs, however, an increasing collector distance is required to prevent the upper layer fibers of the sample from forming defects[18] due to an increasing proximity to the printhead. With this layer-by-layer increase in the collector distance, the HV was left unchanged for a decreasing electric field (**Figure 2**A), while an increasing electric field was adopted without changing the collector distance and incrementally increased HV (Figure 2B). Last, a constant electric field was achieved by incrementally increased[18] collector distance and HV (Figure 2C).

2.1. Control Group

One strength of MEW is that, at minimal build heights, it is a stable process with predictable and reproducible printing outcomes. This is reflected in Figure S2, Supporting Information, where all process parameters remained constant throughout the experiment, reflective of the process stability observed in many previous studies.[15–17,19] The vast majority of previous research papers on MEW, however, use less than 50 fiber layers,[1] and in-process measurements of the Taylor cone area (Figure S2A, Supporting Information) and jet angle (Figure S2B, Supporting Information) for both 0.4 and 0.7 bar confirms a good stability of the process, although the fiber diameter (Figure S2C, Supporting Information) gradually drifted lower at 0.7 bar with a decrease of 2.2 µm over 50 layers. With increasing proximity of the construct to the printhead with a greater number of layers, however, excessive fusion causes disruption in fiber deposition leading to uncontrolled defects (Figure S3, Supporting Information). Where thicker constructs are required, the collector distance must be increased during the printing process to mitigate these deposition errors.

2.2. Decreasing Electric Field

When increasing the collector distance during the print, however, all process signatures commence an oscillatory trend due to a decrease in the electric field over time. First, the Taylor cone (Figure 2D) experienced a steady growth in area before entering into a periodic oscillation behavior at ≈12 min. The amplitude of the oscillation for the mean Taylor cone area kept increasing until the end of experiment. Notably, the comparative amplitude oscillation at 0.7 bar (starting diameter ≈ 16 µm) was greater compared to 0.4 bar (starting diameter ≈ 8 µm).

© 2021 The Authors. Advanced Materials published by Wiley-VCH GmbH

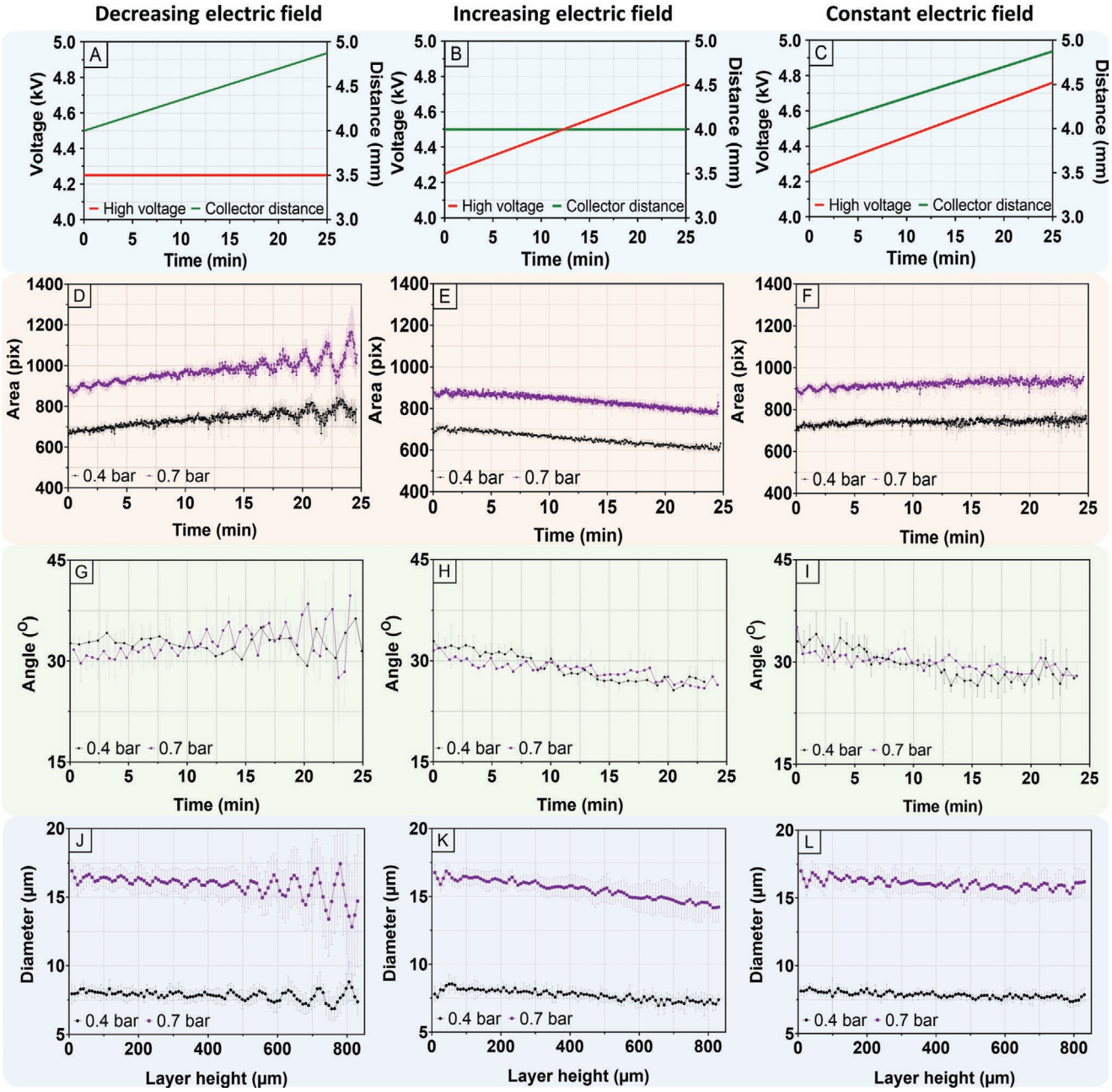

Figure 2. A,D,G,J) Decreasing electric field (A) reveals pulsing behavior across all process signatures (D,G,J). B,E,H) Increasing electric field (B) shows a steady reduction of Taylor cone area (E) and jet angle (H). K) The fiber diameter remained the same at 0.4 bar, while a slow decrease was recorded at 0.7 bar. C,F,I,L) Constant electric field (C) showed no signs of printing instabilities with all process signatures maintaining their level (F,I,L).

The oscillation period was 114 s and 144 s for 0.7 bar and 0.4 bar, respectively. Oscillatory changes in the jet angle were also recorded at both pressures (Figure 2G) and fiber diameter (Figure 2J), starting at the 15 min mark, where the oscillatory frequency matches that of the Taylor cone area.

2.3. Increasing Electric Field

Increasing the electric field during the print gradually reduced the Taylor cone area (Figure 2E). The jet angle (Figure 2H) advanced toward a more vertical shape as the angle value linearly decreased with time. Fiber diameter data shows (Figure 2K) a linear decrease with the increased layers for 0.7 bar. Highlighting the complex and multiparametric nature of MEW, however, a pressure level of 0.4 bar resulted in minimal fiber diameter change.

2.4. Constant Electric Field

A constant electric field compensates for the decreasing nozzle-construct distance by incrementally increasing the collector

© 2021 The Authors. Advanced Materials published by Wiley-VCH GmbH

distance (either 8 or 16 μm for each layer depending on the pressure), while also increasing HV to maintain a constant electric field. Although the recorded standard error for this profile is more significant than an increasing electric field, the results from both 0.4 bar and 0.7 bar (Figure 2F,I,L) do not reveal oscillations in the process signatures. In contrast to a standard electric field, the fiber diameter measurement at both pressures remained constant. This finding further emphasizes the effect of the nozzle-construct distance on the fiber diameter with increased layers.

2.5. Taylor Cone Area

The Taylor cone area and therefore its volume, is related to the changing electric field. The process signature clearly responded to both decreasing and increasing electric field profiles demonstrating that large Taylor cone area amplitude oscillations indicate larger variations in fiber diameter; low Taylor cone area amplitude oscillations indicate smaller variations in fiber diameter. Additionally, the results indicate that increasing the electric field exerts a stronger electrostatic force on the Taylor cone reducing its volume and therefore the Taylor cone area. Last, during constant electric field environment and standard conditions, the Taylor cone area remains unchanged due to the preservation of the electric field throughout the printing process. In summary, monitoring the Taylor cone provides useful real-time information about both stability and fiber diameter.

2.6. Jet Angle

Jet angle results are in line with the Taylor cone area data, albeit with a slight delay of ≈10 s. Although jet angle showed the same trend as Taylor cone area, the recorded standard error is much larger. Frequently changing printing direction and fiber deposition onto uneven surfaces can cause distortion in the jet angle movements. Nevertheless, jet angle is still an important process signature as it not only confirms fiber pulsing instability, yet also estimates the critical translation speed of the jet.

2.7. Fiber Diameter

Finally, fiber diameter measurements confirm the findings from the previously discussed process signatures. Decreasing electric field results confirm that by observing the behavior of the Taylor cone area and jet angle, we were able to analyze whether the printing process experienced unwanted pulsing instability of fiber diameter. The increasing electric field resulted in a reduction in fiber diameters; 1.5 μm per 100 layers for 0.4 bar and 2.6 μm per 50 layers for 0.7 bar (Figure 2K). A similar behavior of fiber diameter was recorded for the standard conditions where both the HV and collector distance did not change over time (Figure S2C, Supporting Information). For these two electric field regimes, the nozzle-construct distance decreased with each printed layer, which suggests that nozzle-construct distance had greater influence on fiber diameter than the electric field. This was confirmed by constant electric field results, where the collector distance was increased with each printed layer to maintain the nozzle-construct distance, thus keep fiber diameter constant.

2.8. Adopting Conditions for MEW Tubes

The majority of MEW studies use a flat collector, with straight fiber deposition.[1,15–18] In this configuration, small changes in the jet lag do not manifest into notable printing defects, partly due to an autofocusing effect where the incoming fiber is attracted to the one that is previously deposited.[19] The fabrication of highly resolved tubular MEW scaffolds, however, is substantially more challenging, as small changes in the jet angle affect the turning point on the mandrel (Figure S4, Supporting Information). It is notable that the tubular MEW studies shown to date have irregular fiber placement[20,21] or are limited to a maximum of 10 total fiber layers.[22–24]

MEW printing parameters require constant changing to maintain stable printing conditions particularly with increasing fiber layers and construct thickness. The improved conditions determined here using MV were transferred to a mandrel configuration, and tubular constructs fabricated with constant electric fields. Constructs with winding angles ranging from 40° to 80° are showing in Figure S5, Supporting Information. **Figures 3**A–F show SEM images of a 80-layer, 100-layer, and 150-layer tubular constructs; These are substantially greater than the thickest accurately fabricated MEW tube to date, which is only 10-layers.[22] Due to the stability of the jet, the ends of the tubes are well-defined and fibers accurately positioned, as the turning point on the mandrel is the location where defects due to jet lag appear.[22,23]

With well-positioned fibers MEW into thin sheets to such thicknesses, they displayed an elastic snap-through instability[25] associated with mechanical metamaterials.[26] The interwoven walls of the MEW tube snap-through into a position mechanically stable enough to mount and visualize with SEM (Figure 3G). Furthermore, 300-layer MEW tubes could be fabricated (Figure 3H,I), which require exceptional accuracy and printing stability of the jet, and tubes continue to demonstrate distinct elastic snap-through mechanical properties. The various stages of snap-through are shown in Figure 3J and in Video S5, Supporting Information. Such snap-through properties have been identified to be important for soft-robotics applications,[27] and this study shows for the first time that MEW-fabricated products can demonstrate this property and is due to the increased layers. Compressing such MEW tubes end-on-end results in a collapsible material with either recovering or lockable positions, depending on the extent of compression (Video S5, Supporting Information). The manufacture of such well-defined MEW tubes is a result of fitting suitable constant electric field parameters.

3. Conclusions

The Taylor cone volume was identified as an important process signature fiber for fabrication quality for MEW. Analysis of

© 2021 The Authors. Advanced Materials published by Wiley-VCH GmbH

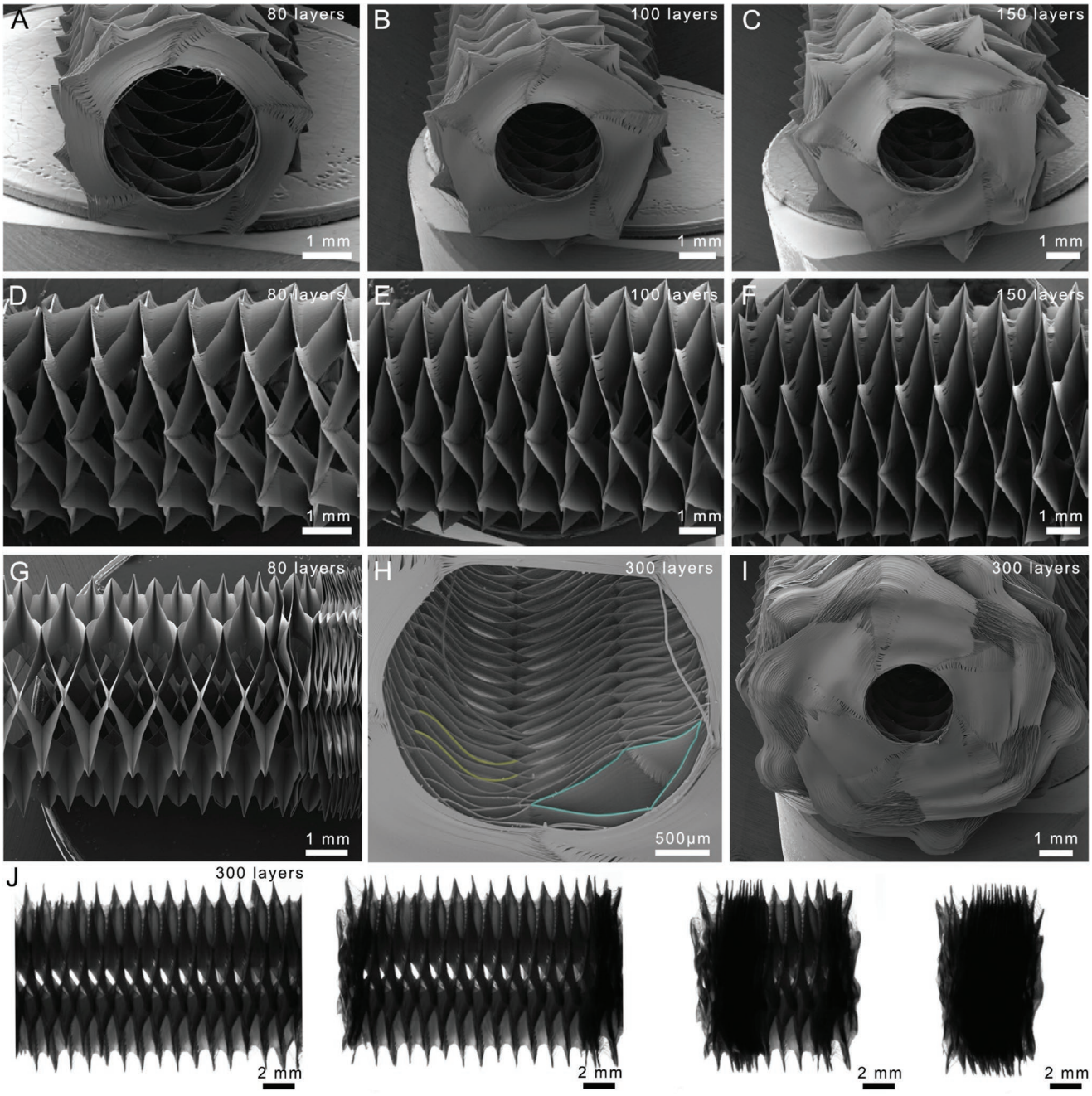

Figure 3. Implementation of MV information for MEW of thick tubes at 60° winding angle. A–C) SEM images of the ends of MEW tubes with 80 (A), 100 (B), and 150 (C) layers. D–F) SEM images showing the longitudinal morphology of MEW tubes with 80 (D), 100 (E), and 150 (F) layers. G) SEM image showing a partially collapsed thick tube. H) SEM image of inside the lumen of a compressed 300-layer MEW tube with false-color yellow indicating the buckling of the fiber walls and false-color blue highlighting a non-collapsed pore. I) SEM image of a challenging 300-layer MEW tube which requires accuracy, control, and printing stability for fabrication. J) Stereomicroscopy images of a 300-layer tube at various states of compression down to ≈20% of its original length.

the jet during MEW using a MV approach led to an improved control protocol of the electric field for the manufacturing of thicker layer constructs. To demonstrate the efficacy of the approach, thick tubular structures were fabricated by achieving constant electric field conditions to achieve build heights that go far beyond current state-of-the-art. Such control is an important advancement in the technology by providing real-time information about printing instabilities which can be subsequently controlled to print complex structures and parts. This investigation demonstrates the importance of real-time monitoring system for MEW, since it is a multiparametric AM technology. This also moves the technology closer to closed-loop control which, as shown for metal-based AM, accelerated its TRL significantly.

© 2021 The Authors. Advanced Materials published by Wiley-VCH GmbH

4. Experimental Section

Material: Medical-grade poly(ε-caprolactone) (PURASORB PC 12, Lot# 1412000249, 03/2015) was obtained from Corbion Inc, Netherlands and used after appropriate storage.[12]

MEW Processing: A custom-built MEW printer shown in Figure 1A,B with both flat and tubular printing capabilities was operated as previously described.[22] The 20 × 70 mm rectangular stainless-steel flat collector and mandrel system were positioned below a MEW head attached to a *z*-axis (Aerotech, Pittsburgh, PA, USA). A 22G nozzle and syringe (3 mL; Nordson Deutschland GmbH, Germany) was used for all samples, and polymer heated and maintained at 89 °C using a custom electrical contoller (JUMO, Germany) in a 21 ± 2 °C ambient temperature, with a relative humidity of 40 ± 10%. A positive voltage source was used, while the pressure was regulated with a manometer. Each print started with a 4.0 mm collector distance.

For experiments involving in-process input parameter adjustment, the change in voltage or collector distance was made for each printed layer. The voltage was adjusted according to the rate of 0.58 kV mm^{-1}.[18] For pressure levels of 0.4 and 0.7 bar, collector distance increases were defined by the predetermined fiber diameter for each layer, measured as 11 and 17 µm respectively, to maintain the nozzle-construct distance. Similarly, the collector was adjusted daily to keep the same critical translation speed across the experiments.

Printing on Flat Collector: A continuous "U" shaped printing path was designed (Figure 1C) to allow a sufficient length for fiber pulsing to occur within a single layer on a small flat metallic collector (20 × 70 mm), and to correlate the image capture time with precise SEM measurements. A section along each of the four walls was chosen for both jet imaging and fiber diameter measurement, as animated in Video S6, Supporting Information.

Printing on a Mandrel: All experiments were performed on the same MEW printer (Figure 1A,B) with a grounded rotating mandrel (diameter; 3 mm) coupled to a DC motor (Aerotech, Pittsburgh USA) with an encoder attached to enable precise digital tracking of the mandrel's speed and position (0.36° ± 0.18°). The precise movements were calculated using an open source MEWTubes application found here (http://mewtubes.herokuapp.com/).[22] A starting voltage of +4.50 kV and collector distance of 4.0 mm was adopted with 0.7 bar used for all tubular prints, otherwise fiber pulsing would occur (Figure S6, Supporting Information).

Camera Visualization: A high-resolution camera was used to capture the jet flight path and was positioned behind a USB camera that provided approximate positioning at start-up. The high-resolution camera (Alpha 7 III, Sony Corporation, Japan) and telescopic lens (ED AF Micro NIKKOR 200 mm lens, Nikon Corporation, Japan) were mounted horizontally at 110 mm from the MEW nozzle (Supporting Information. Each video was started upon finalization of jet stabilization and recorded for the whole duration of printing (25 min). Video S6, Supporting Information shows the regions of the printing process that were used to evaluate the process signatures.

Process Signature Definition: In this study, three process signatures were analyzed; the Taylor cone area, jet angle, and fiber diameter. The Taylor cone refers to a volume of polymer at the nozzle (Figure 1G). Since the Taylor cone and the fiber jet boundary cannot be clearly defined, the cross-sectional area of the polymer between the tip of the nozzle and 60 pixels below the nozzle was used. This value was chosen based on the analysis of various pixel distances from the nozzle (Figure S7, Supporting Information). The fiber jet angle is defined as the angle between the end of the nozzle and the point where the fiber is deposited on the collector, and similarly was based on preliminary segmentation analysis (Figure S8, Supporting Information). The fiber diameter of the direct-written fibers was measured using a SEM of the "U" shaped printed construct at a known position (Figure 2B).

Software Characterization: An image analysis algorithm developed in MALTAB was used to determine the Taylor cone size and the angle of the jet flight path in real-time using different distant extrapolation models from the tip of the nozzle (Figure S9, Supporting Information). A threshold was applied to images to convert them to binary to trace the fiber jet and measure the angle between the tip of the nozzle and the deposition point on the collector. An accurate tracing of different points along the jet verifies the point of deposition to determine the angle (Figure S10, Supporting Information). The angle values were calculated with 50 fps and collected into raw data, which resulted in more than 14 580 data points per print.

Imaging: To determine the *z*-axis adjustments, samples were examined with a stereomicroscope (Zeiss steREO Discovery V2.0 microscope, Oberkochen, Germany) and measurements recorded with the instrument software (Zeiss Zen Blue, Oberkochen, Germany). For each sample fibers were selected at random and five measurements were taken along the length. These calculations were used to determine *z*-axis adjustments when printing as well as for imaging of the tubular constructs. SEM was carried out using a Crossbeam 340 SEM (Carl Zeiss Microscopy, Göttingen, Germany) equipped with a Zeiss Gemini column, to further investigate the fiber diameter and construct morphology. Prior to analysis, all samples were coated (thickness; 4 nm) with platinum using a Leica EM ACE600 high vacuum sputter coater.

Supporting Information

Supporting Information is available from the Wiley Online Library or from the author.

Acknowledgements

P.M. and T.M.R. contributed equally to this work. The technical assistance of Andrei Hrynevich for programming, Dr. Tomasz Jungst for camera provision, and Dr. Philipp Stahlhut for the quality SEM imaging is appreciated. The authors appreciate the EACEA program BIOFAB (grant# 2013/3137 001-001) that supported T.M.R., the financial support of the German Research Foundation (DFG) (project number 322483321) and the Australian Research Council Industrial Transformation Training Centre (external ref: IC160100026, Queensland University of Technology).

Open access funding enabled and organized by Projekt DEAL.

Conflict of Interest

The authors declare no conflict of interest.

Data Availability Statement

The data that support the findings of this study are available from the corresponding author upon reasonable request.

Keywords

3D printing, digitization, electrohydrodynamic, melt electrospinning writing, polycaprolactone

Revised: April 16, 2021
Published online: June 8, 2021

[1] T. M. Robinson, D. W. Hutmacher, P. D. Dalton, *Adv. Funct. Mater.* **2019**, *29*, 1904664.
[2] Á. G. Marín, D. Lohse, *Ph ys. Fluids* **2010**, *22*, 122104.
[3] E. George, P. Liacouras, F. J. Rybicki, D. Mitsouras, *RadioGraphics* **2017**, *37*, 1424.

© 2021 The Authors. Advanced Materials published by Wiley-VCH GmbH

[4] P. Sitthi-Amorn, J. E. Ramos, Y. Wang, K. Joyce, J. Lan, W. Wang, W. Matusik, *ACM Trans. Graphics* **2015**, *34*, 11.
[5] M. Aminzadeh, T. Kurfess, in, *Vision-Based Inspection System for Dimensional Accuracy in Powder-Bed Additive Manufacturing*, ASME, New York **2016**.
[6] W. P. Syam, R. Leach, K. Rybalcenko, A. Gaio, J. Crabtree, *Proc. CIRP* **2018**, *75*, 108.
[7] K. Okarma, J. Fastowicz, in *Computer Vision Methods for Non-destructive Quality Assessment in Additive Manufacturing*, Springer, Cham, Switzerland **2020**, pp. 11–20.
[8] B. M. Colosimo, M. Grasso, *J. Qual. Technol.* **2018**, *50*, 391.
[9] W. Cui, Y. Zhang, X. Zhang, L. Li, F. Liou, *Appl. Sci.* **2020**, *10*, 545.
[10] F. M. Wunner, P. Mieszczanek, O. Bas, S. Eggert, J. Maartens, P. D. Dalton, E. M. De-Juan-Pardo, D. W. Hutmacher, *Biofabrication* **2019**, *11*, 025004.
[11] A. Hrynevich, B. S. Elci, J. N. Haigh, R. McMaster, A. Youssef, C. Blum, T. Blunk, G. Hochleitner, J. Groll, P. D. Dalton, *Small* **2018**, *14*, 1800232.
[12] G. Hochleitner, A. Youssef, A. Hrynevich, J. N. Haigh, T. Jungst, J. Groll, P. D. Dalton, *BioNanomaterials* **2016**, *17*, 159.
[13] F. Chen, G. Hochleitner, T. Woodfield, J. Groll, P. D. Dalton, B. G. Amsden, *Biomacromolecules* **2016**, *17*, 208.
[14] D. Nahm, F. Weigl, N. Schafer, A. Sancho, A. Frank, J. Groll, C. Villmann, H. W. Schmidt, P. D. Dalton, R. Luxenhofer, *Mater. Horiz.* **2020**, *7*, 928.
[15] F. Tourlomousis, C. Jia, T. Karydis, A. Mershin, H. Wang, D. M. Kalyon, R. C. Chang, *Microsyst. Nanoeng.* **2019**, *5*, 15.
[16] K. F. Eichholz, D. A. Hoey, *Acta Biomater.* **2018**, *75*, 140.
[17] N. T. Nguyen, J. H. Kim, Y. H. Jeong, *Mater. Sci. Eng., C* **2019**, *103*, 109785.
[18] F. M. Wunner, M. L. Wille, T. G. Noonan, O. Bas, P. D. Dalton, E. M. De-Juan-Pardo, D. W. Hutmacher, *Adv. Mater.* **2018**, *30*, 1706570.
[19] H. Ding, K. Cao, F. Zhang, W. Boettcher, R. C. Chang, *Mater. Des.* **2019**, *178*, 107857.
[20] T. D. Brown, A. Slotosch, L. Thibaudeau, A. Taubenberger, D. Loessner, C. Vaquette, P. D. Dalton, D. W. Hutmacher, *Biointerphases* **2012**, *7*, 13.
[21] A. M. van Genderen, K. Jansen, M. Kristen, J. van Duijn, Y. Li, C. C. L. Schuurmans, J. Malda, T. Vermonden, J. Jansen, R. Masereeuw, M. Castilho, *Front. Bioeng. Biotechnol.* **2020**, *8*, 2296.
[22] E. McColl, J. Groll, T. Jungst, P. D. Dalton, *Mater. Des.* **2018**, *155*, 46.
[23] T. Jungst, M. L. Muerza-Cascante, T. D. Brown, M. Standfest, D. W. Hutmacher, J. Groll, P. D. Dalton, *Polym. Int.* **2015**, *64*, 1086.
[24] T. Jungst, I. Pennings, M. Schmitz, A. J. W. P. Rosenberg, J. Groll, D. Gawlitta, *Adv. Funct. Mater.* **2019**, *29*, 1905987.
[25] M. Gomez, D. E. Moulton, D. Vella, *Nat. Phys.* **2017**, *13*, 142.
[26] X. Yu, J. Zhou, H. Liang, Z. Jiang, L. Wu, *Prog. Mater. Sci.* **2018**, *94*, 114.
[27] H. Lee, Y. Jang, J. K. Choe, S. Lee, H. Song, J. P. Lee, N. Lone, J. Kim, *Sci. Rob.* **2020**, *5*, eaay9024.

© 2021 The Authors. Advanced Materials published by Wiley-VCH GmbH